

# Towards Agile Swarming in Real World: Onboard Relative Localization with Fast Tracking of Active Blinking Markers\*

Tim Lakemann<sup>a,\*</sup>, Daniel Bonilla Licea<sup>a,b</sup>, Viktor Walter<sup>a</sup>, Tomáš Báča<sup>a</sup>,  
Martin Saska<sup>a</sup>

<sup>a</sup>*Czech Technical University, Karlovo namesti 13, Prague, 121 35, Czech Republic*

<sup>b</sup>*Mohammed VI Polytechnic University, Morocco*

---

## Abstract

A novel onboard tracking approach enabling vision-based relative localization and communication using Active blinking Marker Tracking (AMT) is introduced in this article. Active blinking markers on multi-robot team members improve the robustness of relative localization for aerial vehicles in tightly coupled swarms during real-world deployments, while also serving as a resilient communication channel. Traditional tracking algorithms struggle to track fast moving blinking markers due to their intermittent appearance in the camera frames. AMT addresses this by using weighted polynomial regression to predict the future appearance of active blinking markers while accounting for uncertainty in the prediction. In outdoor experiments, the AMT approach outperformed state-of-the-art methods in tracking density, accuracy, and complexity. The experimental validation of this novel tracking approach for relative localization involved testing motion patterns motivated by our research on agile multi-robot deployment.

*Keywords:* Visual Tracking, Localization, Multi-Robot Systems, Computer Vision for Automation

---

## 1. Introduction

In various applications, collaborative multi-Unmanned Aerial Vehicle (UAV) systems enhance redundancy and improve efficiency compared to single-robot

---

\*This work was funded by CTU grant no SGS23/177/OHK3/3T/13, by the Czech Science Foundation (GAČR) under research project no. 23-07517S and by the European Union under the project Robotics and advanced industrial production (reg. no. CZ.02.01.01/00/22\_008/0004590).

\*Corresponding author, +420-22435-7255

*Email address:* lakentim@fel.cvut.cz (Tim Lakemann)



Figure 1: Six agile swarm members flying in challenging desert conditions, relying on UVDAR-based relative localization as used in this work.

systems [1]. Accurate localization of team members is crucial for collision avoidance and effective collaborative task execution [1, 2]. Global Navigation Satellite System (GNSS) alone is insufficient for close formation flight in such environments due to its meter-level accuracy, limited availability (e.g., indoors, underground), and vulnerability to jamming and spoofing [3, 4]. While Real-Time Kinematic (RTK)-GNSS and motion capture systems offer centimeter-level accuracy, they rely on external infrastructure or public networks, limiting their practicality in many real-world environments [1, 2, 5]. Alternatively, onboard Ultra-wideband (UWB) provides comparable precision in distance estimation without requiring external infrastructure. However, its effectiveness can be limited by radio jamming, interference, and channel saturation, and for pose measurements, a UWB network with external anchors is required [3, 6, 7, 8]. Camera-based mutual relative localization offers a robust and cost-efficient solution for multi-robot systems without external infrastructure [9]. This method of relative localization relies on camera-based object detection and tracking algorithms. In recent works [3, 9, 10], such algorithms often use Convolutional Neural Networks (CNNs), which are computationally intensive, have low output rates on general purpose PCs, are highly dependent on illumination, and are typically limited to the specific robot platforms included in the training dataset. Passive markers attached to robot platforms for visual localization are cost-effective and easy to deploy in multi-robot systems [11, 12]. However, they are also dependent on illumination and require planar surfaces for attachment, which is impractical for small robots. To overcome these limitations, active markers in the form of Light-Emitting Diodes (LEDs) can be attached to team members, allowing for efficient background separation and reliable operation in challenging outdoor/indoor environments [13, 14, 15, 16, 17, 18]. When using constant power, the markers are visible in consecutive camera frames, allowing for the use of classical tracking algorithms, such as the Kalman filter [19, 20, 21]. This reduces team member differentiation and increases the risk of false detections from outdoor sunlight, reflections, and indoor artificial lighting.

These challenges may be overcome by modulating the blinking frequencies of the markers. By using, e.g. On-Off Keying (OOK), the team members can

share information and uniquely identify each other [14, 22, 23, 24, 25]. Conventional tracking algorithms are inadequate for tracking active blinking markers due to their intermittent appearance and movement in the camera image of the Receiver (RX), which is caused by relative motion between team members [26]. Additionally, recent studies on agile multi-robot teams have shown maximum trajectory speeds of  $2 \text{ m s}^{-1}$  in object-dense outdoor environments [8], and  $7.4 \text{ m s}^{-1}$  in object-sparse indoor environments using external infrastructure, such as a motion capture system [27]. Even at lower inter-agent speeds, effective tracking algorithms are crucial for relative localization, as relative motion within these teams surpasses the abilities of current state-of-the-art methods.

We propose the novel AMT approach, a system-agnostic method for tracking light sources attached to multi-robot team members. By using motion models and the constraints of cooperating aerial robots, the AMT approach solves the tracking problem by fusing the past motion of blinking light sources to estimate the next expected location of the team members in the image. This proposed approach enables vision-based relative localization of blinking light sources attached to fast moving UAVs (Fig. 1). The source code<sup>1</sup> and a demonstration video<sup>2</sup> can be found online.

## 2. State of the Art and Contribution

Active blinking markers attached to the UAV frame enhance reliability and enable unique identification, while also reducing the computational cost of object detection algorithms. In [14], White *et al.* tracked a static LED ring using spatial-temporal difference images, with the ring blinking at half the frame rate of the camera. This work was extended in [22] by attaching the LED ring to a UAV and tracked it with a stationary camera. However, using difference images restricts the blinking frequency for all team members to half the frame rate of the camera, making it difficult to distinguish between the transmitting UAVs (TXs).

Breitenmoser *et al.* developed a mutual relative localization system using active and passive markers in [28], achieving centimeter-level accuracy in indoor experiments. However, they observed that different marker frequencies could enhance robustness in differentiating robot targets. Additionally, the system was not tested for cross-talk detection when robots were close.

In [24, 25, 29, 30], the authors tracked a UAV with blinking markers using a Dynamic Vision System (DVS), which requires different tracking approaches compared to Complementary Metal-Oxide-Semiconductor (CMOS) cameras. Cenci *et al.* extracted the individual frequencies associated with Infrared (IR)-markers attached to a UAV in an indoor environment [29]. In [30], a DVS was used to

---

<sup>1</sup><https://github.com/TimLakemann/ami.git>

<sup>2</sup><https://mrs.fel.cvut.cz/towards-agile-swarming-in-real-world>

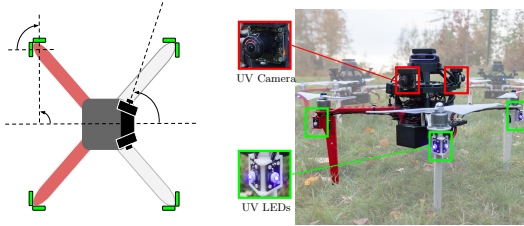


Figure 2: UAV equipped with the UVDAR system [36].

track a marker board with four blinking LEDs. They tested the system in indoor and outdoor environments with a working distance of up to 10 meters. However, their system fails to address occlusions or situations where the LEDs appear close together in the image. Further, DVSs typically have a limited Field of View (FOV) and are more expensive than CMOS cameras [31]. To our knowledge, systems using DVSs do not handle tracking when both the RX and TX are moving, making them impractical for mutual relative localization and, consequently, for multi-robot systems.

In [32], the authors changed the light intensity of IR-LEDs to represent the two different bit states. Changes in light intensity are effective in indoor environments. However, it causes ambiguities in outdoor environments due to higher background brightness and noise caused by sunlight.

In [23], the authors used a combination of three blue non-blinking markers for relative localization and one red blinking marker for identification attached to the frame of a UAV for indoor relative localization. This combination enables continuous tracking by the non-blinking markers and unique identification by the blinking markers. However, non-blinking markers reduce transmission bandwidth and reliability. At the same time, reliance on the visible spectrum increases dependence on lighting conditions and limits the operational range of UAVs in outdoor environments.

### 2.1. The UVDAR system

The UVDAR system provides relative localization and communication for UAVs operating in both indoor and outdoor environments [16, 31, 33, 34, 35]. s in varying lighting conditions [31]. The system uses Ultraviolet (UV)-LEDs on the arms of a target UAV for data transmission in combination with calibrated grayscale cameras with UV band-pass filters (Fig. 2) attached on observer UAVs [36]. The band-pass filters remove the most visible light, making the blinking markers appear as bright white spots in the camera image of the observer. These are then processed using a Features from Accelerated Segment Test (FAST)-like procedure and non-maxima suppression to extract the center pixel of each marker [31, 33].

Multiple UV-LEDs on a single multirotor’s arm emit an identical sequence, recognized as a blinking marker (green box in Fig. 2). These binary sequences are

stored in a dictionary  $\mathcal{D}$  that contains LED-IDs associated with each sequence [36]. In our previous work [33], we solved the tracking problem of the blinking markers by using the Hough Transform for 3D line extraction. The search for maxima in the Hough Space introduces high computational load and memory usage. Additionally, the line approximation of the movement of the marker in the image is insufficient for fast and agile maneuvers of the multi-robot system.

## 2.2. Contribution

This work is motivated by the need for reliable mutual visual tracking in agile multi-robot systems operating in real-world (outdoor/indoor) environments, particularly in tightly cooperating swarms. The proposed approach was integrated with the UltraViolet Direction And Ranging (UVDAR) system [31], but it can also be applied to any multi-robot framework using active blinking markers. We validated its effectiveness through outdoor experiments, demonstrating substantial performance improvements over the state-of-the-art method. The main contributions of this work are the following:

1. We propose a novel approach for tracking blinking markers across consecutive images, considering the requirements of onboard mutual relative localization under the constraints of agile flight.
2. We use uncertainty estimates from weighted polynomial regression to define a search window for future marker appearances, enhancing tracking accuracy under dynamic conditions.
3. We propose a recovery mechanism that re-tracks blinking markers after tracking failures, significantly increasing reliability for the real-world deployment of closely cooperating teams.
4. We provide an enabling technology for fast, agile aerial multi-robot systems with vision-only relative localization.

## 3. Active blinking Marker Tracking (AMT)

The proposed AMT approach enables the tracking of multiple moving blinking light sources across consecutive image captures, allowing the extraction of individual blinking sequences, which is essential for agile multi-UAV systems. Positions of extracted bright points (see Sec. 2.1) from a recent camera image are stored in the set  $\mathcal{P}_t = \{p_{t,1}, \dots, p_{t,k}, \dots, p_{t,m}\}$ , where  $t$  is the timestamp of the image acquisition. These positions are referred to as *image-points*.

The AMT approach requires knowledge of the maximum number of consecutive zeros ( $b_{m,0}$ ) of the sequences emitted by the blinking markers; this is necessary to keep only valid entries in the dynamic buffer, named  $\mathcal{B}$ . The buffer  $\mathcal{B}$  tracks potential matches between the *image-points* and sequences emitted by the blinking markers of the TXs and stores the associations in *t-series*. An *image-point* is converted to a point state (*p-state*) as soon as it is inserted into  $\mathcal{B}$ . A *p-state* contains the image capture time, pixel coordinates, and *state*, which can be either ‘1’ (marker “on”) or ‘0’ (marker “off”). Fig. 3 provides an overview of  $\mathcal{B}$  and

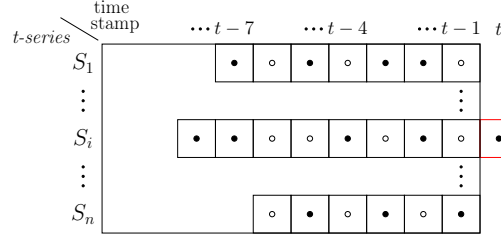


Figure 3:  $\mathcal{B}$  contains multiple  $t$ -series ( $S_1, \dots, S_n$ ), each with multiple  $p$ -states. Black circles indicate “on”-state; white circles indicate “off”-state of blinking marker. Red rectangle: new  $p$ -state inserted into  $S_i$ .

Sec. 3.1 further explains the concept of  $\mathcal{B}$  and  $t$ -series. The AMT approach is divided into three parts:

1. *Local Search* (Sec. 3.2): uses the markers’ expected maximal speed in the image to approximate their next appearance.
2. *Extended Search* (Sec. 3.3): is used for all  $t$ -series for which the *Local Search* has failed. It predicts the next occurrence of a blinking marker based on its past image coordinates.
3. *Verification* (Sec. 3.4): ensures that  $\mathcal{B}$  stays in memory bounds, optimizing computation efficiency.

### 3.1. Dynamic Buffer $\mathcal{B}$

The buffer  $\mathcal{B}$  stores  $p$ -states from a sequence of consecutive camera images, and is used as the basis for the proposed tracking method.  $\mathcal{B}$  contains a set of  $t$ -series - conceptualized as rows, each containing multiple consecutive  $p$ -states associated with the same moving blinking marker. The  $p$ -states in  $\mathcal{B}$  which correspond to the same timestamp are conceptualized as being in the same column (Fig. 3). Each row in  $\mathcal{B}$  can potentially match with a sequence in  $\mathcal{D}$ . A  $t$ -series in the  $i$ -th row of  $\mathcal{B}$  is denoted by  $S_i$ , and the  $p$ -state in  $S_i$  at timestamp  $t - j$  (with  $j$  timestamps before the last image capture at  $t$ ) is written as  $p(S_i)_{t-j}$ . When a new association between  $S_i$  and an *image-point* in  $\mathcal{P}_t$  is found, the *image-point* is appended as a  $p$ -state at the end of  $S_i$  (see red rectangles in Figs. 3 and 4).

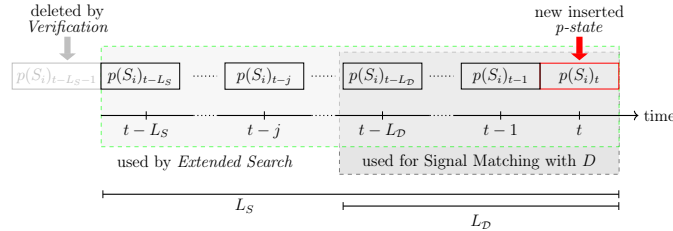


Figure 4:  $t$ -series containing multiple  $p$ -states. Red rectangle: new  $p$ -state inserted at timestamp  $t$ . Green rectangle: Maximal length  $L_S$  of  $t$ -series. *Verification* method removes  $p$ -state surpassing  $L_S$ .

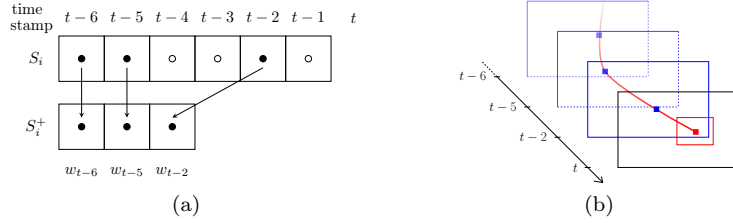


Figure 5: (a) The *Extended Search* selects all  $p$ -states of a  $t$ -series with value ‘1’. (b) Past images (blue) with pixel locations of  $S_i^+$  and polynomial regression (red) with its search window in the image at timestamp  $t$ .

$\mathcal{B}$  uses two boundaries to cope with its dynamic nature: one limits the maximum number of rows, controlling the number of allowed  $t$ -series in the buffer, while the other restricts the maximum columns ( $L_S$ ), defining the maximum length of a  $t$ -series in  $\mathcal{B}$ . The limitation on rows serves as a safety measure to prevent memory overflow. It also counteracts the continuous insertion of new  $t$ -series into  $\mathcal{B}$  in noisy background conditions (e.g. sun reflections on water surfaces), making associations infeasible. The maximum number of columns, corresponding to the number of  $p$ -states per  $t$ -series, is primarily defined by the metrics used in the *Extended Search* (Fig. 4).

### 3.2. Local Search

The *Local Search* matches  $t$ -series in  $\mathcal{B}$  and *image-points* in  $\mathcal{P}_t$  based on the maximal linear movement ( $\Delta p x_m = (\Delta x_m, \Delta y_m)$ ) of a blinking marker between two consecutive frames, with  $\Delta x_m$  and  $\Delta y_m$  describing horizontal and vertical displacements, respectively. The maximal expected displacement of a blinking marker between two frames, in pixel units, is defined as:

$$\Delta p x_m = (\lceil v_{x,\max}/f \rceil, \lceil v_{y,\max}/f \rceil), \quad (1)$$

where  $v_{x,\max}$  and  $v_{y,\max}$  are the maximum horizontal and vertical velocities of a blinking marker in the image, respectively, and are measured in pixels per second over a one-second interval. These values were experimentally determined by analyzing marker motion across frames under varying robot speeds, distances, and relative motion.

For each  $t$ -series in  $\mathcal{B}$ , the *Local Search* constructs a fixed search area around the last inserted  $p$ -state using equation (1). For  $S_i$ , this search area is denoted by  $p(S_i)_{t-1} \pm \Delta p x_m$ . If an *image-point*  $p_{t,k}$  in  $\mathcal{P}_t$  lies in the search area of  $S_i$ ,  $p_{t,k}$  is appended to  $S_i$  as a new  $p$ -state.

This fixed search area works well when the relative movement between the RX and TX causes minimal marker displacement in the image, but it may be insufficient when a UAV performs agile maneuvers. The *image-points* of  $\mathcal{P}_t$  with unsuccessful insertion into  $\mathcal{B}$  by the *Local Search* are stored in the subset  $\mathcal{P}_t^*$ . The subset of  $\mathcal{B}$ , denoted by  $\mathcal{B}^*$ , stores all  $t$ -series with unsuccessful correspondence search by the *Local Search*.  $\mathcal{B}^*$  and  $\mathcal{P}_t^*$  are then used in the *Extended Search*.

### 3.3. Extended Search

The *Extended Search* executes a correspondence search between the  $t$ -series in  $\mathcal{B}^*$  and the *image-points* in  $\mathcal{P}_t^*$ . In  $\mathcal{B}^*$ , it selects for each  $t$ -series only the ‘1’- $p$ -states (blinking marker turned “on”; Fig. 5a), resulting in a discontinuous, shorter  $t$ -series, denoted by  $S_i^+$ . During the ‘1’- $p$ -states the pixel coordinates of the marker are known with a higher precision compared to the ‘0’- $p$ -states (blinking marker turned “off”). On  $S_i^+$ , a weighted polynomial regression is performed by assigning individual weights to each  $p$ -state in  $S_i^+$  using a time-dependent exponential decay function [37]. Applying a numerically stable *QR-Decomposition* using *Householder-reflections* [38] solves the weighted least squares problem, avoiding computationally expensive and potentially numerically unstable matrix inversion [39]. The polynomial regression predicts the pixel coordinates  $\hat{x}$  and  $\hat{y}$  for timestamp  $t$  and is denoted by  $\hat{p}(S_i)_t$ , for the blinking marker represented by  $S_i$ . For each  $t$ -series in  $\mathcal{B}^*$ , an individual search window is constructed based on the uncertainty in computing the regression coefficients, referred to as the prediction interval for a new response [40]. With the Student’s  $t$ -distribution  $(\mathbf{t}_{1-\frac{\alpha}{2}, \nu})$ , the search area around  $\hat{p}(S_i)_t$  for timestamp  $t$  is defined by:

$$\hat{p}(S_i)_t \pm (\mathbf{t}_{1-\frac{\alpha}{2}, \nu}) \sqrt{\hat{\sigma}_w^2 \left( 1 + \frac{1}{L_i^+} + \frac{(t - \bar{t}_w)^2}{\sum_{k=1}^{L_i^+} (t_k - \bar{t}_w)^2} \right)}, \quad (2)$$

where  $\hat{\sigma}_w^2$  denotes the unbiased estimator for the error variance  $\sigma_w$ .  $\bar{t}_w$  represents the weighted mean of all timestamps in  $S_i^+$ , with weights determined by an exponential decay function.  $L_i^+$  is the number of  $p$ -states in  $S_i^+$ ,  $\alpha$  is the desired probability for the critical value from the Student’s  $t$ -distribution, and  $\nu$  is its degree of freedom, defined by:

$$\nu = L_i^+ - (d + 1), \quad (3)$$

where  $d$  denotes the polynomial degree.

The maximum permissible length of a  $t$ -series in  $\mathcal{B}$ , denoted by  $L_S$ , depends on the parameters of the *Extended Search*. The desired polynomial degree  $d$ , crucial for approximating the past movement of a blinking marker, is influenced by the quantity of past  $p$ -states stored in a  $t$ -series. Consequently, a larger  $L_S$  entails accounting for a longer historical trajectory, requiring a higher polynomial degree, and vice versa. This relationship can be expressed by:

$$L_S = \eta d, \quad (4)$$

where  $d$  is the polynomial degree for the regression and  $\eta \in \mathbb{N}^+$  is a parameter chosen through experiments.

Similarly to the *Local Search*, if an *image-point* from  $\mathcal{P}_t^*$  lies in the search window of a  $t$ -series, defined by equation (2), it is appended to the end of that  $t$ -series. The *image-points* from  $\mathcal{P}_t^*$  for which the *Extended Search* did not find



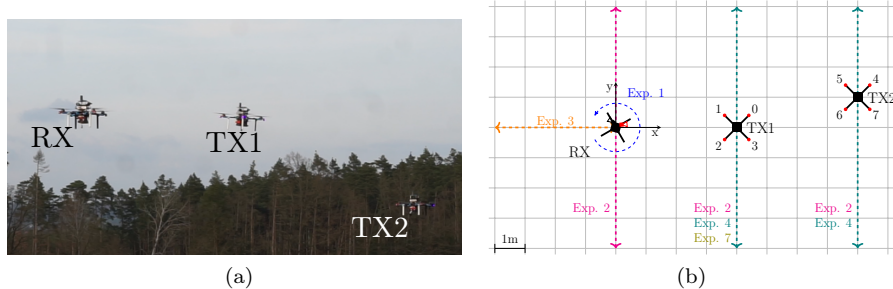


Figure 6: (a) Two Transmitters flying in front of one RX. (b) Experimental Setup: In experiments 2-6, the right camera (red) of the RX points at two TXs flying parallel to the  $y$ -axis. In Experiment 7, only one Transmitter (TX) is used to test the algorithm during agile maneuvers. Numbers around the TXs' arms show the LED-IDs emitted by the blinking markers.

a correspondence in  $\mathcal{B}^*$  are stored in a new set, denoted  $\mathcal{P}_t^\Gamma$ . Similarly,  $t$ -series from  $\mathcal{B}^*$  without new insertions from  $\mathcal{P}_t^*$  are stored in a new set,  $\mathcal{B}^\Gamma$ .

### 3.4. Verification

The *Verification* method contains multiple tasks. If  $\mathcal{B}^\Gamma$  contains  $t$ -series, both correspondence searches failed to find new associations for the stored  $t$ -series in  $\mathcal{B}^\Gamma$ . The AMT approach expects that a blinking marker represented by the  $t$ -series in  $\mathcal{B}^\Gamma$  is either “off” in the image frame at timestamp  $t$  or otherwise not visible. Consequently, for all  $t$ -series in  $\mathcal{B}^\Gamma$ , the pixel coordinates of the  $p$ -states at timestamp  $t - 1$  are duplicated and inserted as new ‘0’- $p$ -states. Since the *Extended Search* ignores ‘0’- $p$ -state, the previous motion is not considered when inserting the ‘0’- $p$ -state. In Fig. 7, a red arrow highlights this process for  $S_i$ .

This could result in continuously inserting  $p$ -states representing ‘0’ bits into  $t$ -series that lack new data associations. This scenario is likely to occur when a blinking marker exits the FOV of the camera or if it becomes occluded, both of which would result in a  $t$ -series containing only ‘0’- $p$ -states. In the *Verification*

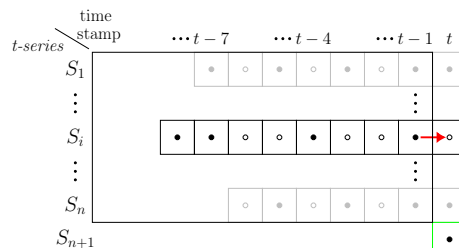


Figure 7:  $S_1$  and  $S_n$  in gray: successful correspondence searches by the *Local Search* or *Extended Search*. Red arrow: duplication of  $p(S_i)_{t-1}$  to ‘0’- $p$ -state at timestamp  $t$ . Green rectangle: initialization of a new  $t$ -series at the end of  $\mathcal{B}$ .

method, the validity of each  $t$ -series in  $\mathcal{B}$  confirms the condition

$$\sum_{j=t-(e+b_{m,0})}^t p_{\mathbf{s}}(S_i)_j \geq e + b_{m,0} \quad \{i \in \mathcal{B}\}, \quad (5)$$

with  $p_{\mathbf{s}}(S_i)_j$  denoting the **state** of  $p(S_i)$  at timestamp  $j$ , and  $e$  denoting the expected bit error rate per sequence transmission. If the condition (5) is violated for a  $t$ -series due to continuous ‘0’- $p$ -state insertions, the *Verification* method deletes the  $t$ -series from  $\mathcal{B}$ . To re-track a blinking marker after a tracking failure caused by situations such as obstruction by an object, the value of  $e$  should be set sufficiently high to keep the invalid  $t$ -series in the buffer. This allows for re-tracking the blinking marker by the *Extended Search*. However, by increasing the value of  $e$ , the overall computational cost and memory usage increases since invalid  $t$ -series are kept longer in  $\mathcal{B}$  until condition (5) is violated. Additionally, the *Verification* method deletes the  $p$ -states in a  $t$ -series that surpass the maximum number of columns,  $L_S$ , preventing memory overflow (Fig. 4).

Each *image-point* in  $\mathcal{P}_t^{\Gamma}$  is inserted as a new  $t$ -series into  $\mathcal{B}$ , thereby increasing the numbers of rows by the length of  $\mathcal{P}_t^{\Gamma}$ , allowing the algorithm to track newly appearing blinking markers in the FOV of the camera. Fig. 7 depicts this process for a single *image-point* by the green rectangle.

Consequently by this point, all *image-points* in  $\mathcal{P}_t$  have been inserted into  $\mathcal{B}$ , either by the *Local Search*, *Extended Search*, or *Verification* method.

#### 4. Experimental Evaluation

We evaluated the AMT approach in outdoor experiments, comparing it with the state-of-the-art 4D Hough Transform (4DHT) approach [33] used in the previous version of the UVDAR system. A quadrotor UAV based on the *Holybro X500* platform was used with an *Intel NUC 10 i7FNK* (6 cores, up to 4.7 GHz; details in [41]). Both onboard and offline executions showed indiscernible performance differences. Therefore, we re-executed both algorithms on the same computer (*Intel i7-8550U* CPU, 1.8 GHz) and dataset for a fair comparison. This paper presents the seven most relevant experiments from a set of 14 involving two/three UAVs (Fig. 6). Each trajectory in each experiment was flown in a periodic loop, with a minimum duration of 60 s.

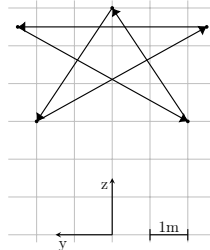


Figure 8:  $y$ - $z$  coordinates for TX1 and TX2 during “star” trajectory in Exp. 6.

Exp. 1: TX1 and TX2 hovered at distances of 4.12 m and 8.06 m from the RX, respectively. The RX rotated around its yaw axis, causing the blinking markers of the TXs to move in a linear horizontal trajectory within the image.

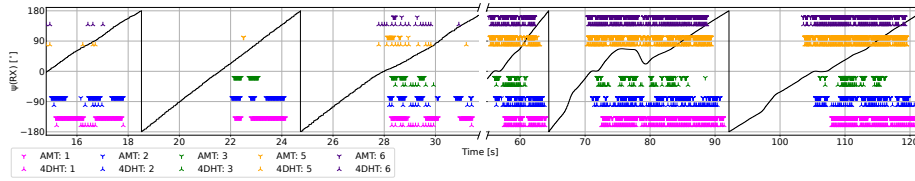


Figure 9: Experiment 1: Yaw angle ( $\psi$ ) of RX with extracted LED-IDs.

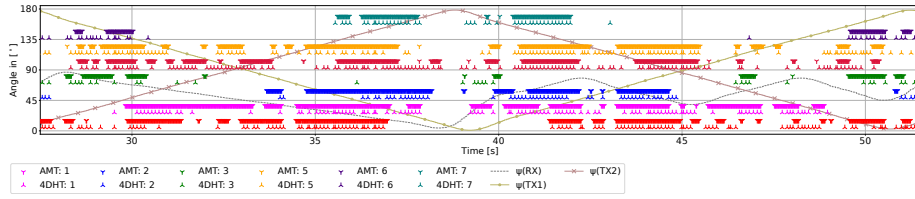


Figure 10: Experiment 2: Yaw angle ( $\psi$ ) of RX and TXs with extracted LED-IDs.

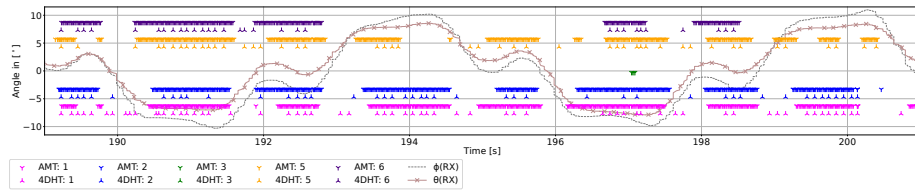


Figure 11: Experiment 3: Roll ( $\phi$ ) and Pitch ( $\theta$ ) angle of RX with extracted LED-IDs.

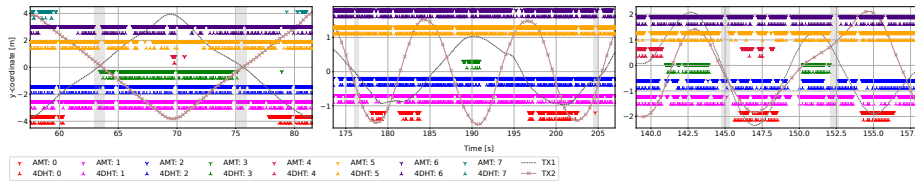


Figure 12: Extracted LED-IDs with y-coordinates for TX1 and TX2 in linear (Exp. 4; left), circular (Exp. 5; center), and "star" (Exp. 6; right) trajectories. Gray areas highlight when the TXs were close in the image.

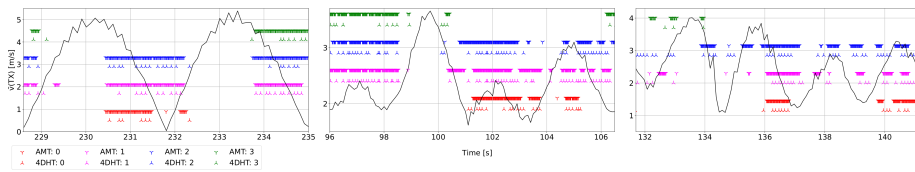


Figure 13: Experiment 7: Extracted LED-IDs with a relative velocity of TX1 during the fastest linear (left), circular (center), and "star" (right) trajectories.

Exp. 2: All UAVs followed a parallel linear trajectory of 8 m (Fig. 6b), with the TXs rotating 180 degrees and the RX rotating between 0 and 90 degrees. The rotations introduced additional horizontal movement and signal crosstalking when two blinking markers of one TX were close in the image due to its rotation.

Exp. 3: Similar to Exp. 1, the TXs hovered at minimum relative distances of 4.12 m and 8.06 m from the RX, and at maximum relative distances of 8.06 m and 12.04 m from the RX for TX1 and TX2, respectively. The RX followed a linear trajectory of 4 m in the  $x$ -direction, causing vertical motion of the TXs markers in the image and testing the algorithm’s response to abrupt deceleration and acceleration of the markers in the image.

Exp. 4: TX1 and TX2 followed linear trajectories of 8 m perpendicular to the RX’s camera optical axis. TX1 had a minimum relative distance of 4 m and a maximum relative distance of 5.66 m, while TX2 had a minimum relative distance of 8 m and a maximum relative distance of 8.94 m, resulting in linear motion of the blinking markers in the image with sudden stops at the endpoints. The maximum velocities of TX1 and TX2 were  $1.19 \text{ m s}^{-1}$  and  $1.54 \text{ m s}^{-1}$ , respectively. This experiment also introduced occlusions of TX2 by TX1 at the center of their trajectories.

Exp. 5: The TXs followed circular trajectories, with TX1 having a radius of 1 m, a maximum velocity of  $0.6 \text{ m s}^{-1}$ , and a relative distance of 4.12 m from the RX. TX2 had a radius of 1.5 m, a maximum velocity of  $1.44 \text{ m s}^{-1}$ , and a relative distance of 8.14 m from the RX. This experiment evaluated the algorithm’s performance on curved paths and during occlusions caused by TX1, adding complexity when both TXs were close together in the image.

Exp. 6: The TXs followed a “star” trajectory (Fig. 8), with TX1 at 4 m and TX2 at 8 m distance along the  $x$ -axis, resulting in the most complex motions in the image. TX1’s maximum velocity was  $2.22 \text{ m s}^{-1}$ , while TX2’s was  $1.63 \text{ m s}^{-1}$ .

Exp. 7: In this experiment, TX1 was the only transmitter. We flew similar trajectories to Exp. 4-6 at two different speeds to evaluate the AMT approach for agile multi-robot systems. For the linear trajectory, TX1 reached relative maximum speeds of  $2.40 \text{ m s}^{-1}$  and  $5.43 \text{ m s}^{-1}$ ; for the circular trajectory,  $2.57 \text{ m s}^{-1}$  and  $4.06 \text{ m s}^{-1}$ ; and for the “star” trajectory,  $3.85 \text{ m s}^{-1}$  and  $4.39 \text{ m s}^{-1}$ .

Tab. 1 shows the parameters selected for the AMT approach during the experiments. Figs. 9 – 13 present excerpts from the experiments to enhance readability and facilitate comparison between the two approaches. The colored markers represent the tracked LED-IDs by the AMT and 4DHT approach alongside trajectory information of the moving UAVs. In Fig. 9, results from experiment 1 include the extracted LED-IDs and the RX yaw angle ( $\psi(RX)$ ). Both approaches failed to extract LED-IDs 0, 4, and 7 as these were oriented away from the RX. Two rotational speeds were tested:  $1.01 \text{ rad s}^{-1}$  and  $0.28 \text{ rad s}^{-1}$ . During the flight with the faster rotations (first excerpt in Fig. 9), the 4DHT approach outperformed the AMT approach for LED-IDs 5 and 6 at timestamp  $t = 15$ . The AMT approach outperformed the 4DHT approach for all LED-IDs

Symbol / Exp.	1+2	3-6	7	Symbol / Exp.	1+2	3-6	7
$f$ [fps]	60	60	60	$\alpha$ [%]	80.0	95.0	95.0
$b_{m,0}$ [bits]	10	10	10	$L_{\mathcal{D}}$ [bits]	18	18	18
$e$ [bits]	0	0	0	$L_S$ [bits]	360	360	360
$\lambda$	1.0	0.1	0.1	$d$	1	4	3
$x_m$ [pixels]	0	6	12	$\eta$	360	90	120
$y_m$ [pixels]	14	6	12				

Table 1: Parameters used by the AMT approach.

at timestamp  $t = 22$ . Fig. 10 shows the  $y$ -coordinates and rotations of all UAVs with the extracted LED-IDs by both approaches. During the experiment, the AMT approach had a better tracking performance compared to the 4DHT approach.

Experiments 1 and 2 showed that even during maximal linear horizontal motions of blinking markers in the image of the observer, the AMT approach can still track the UAVs, performing similarly to or better than the 4DHT approach.

For experiment 3, the performance of the two approaches is shown in Fig. 11 alongside the roll ( $\phi_x(RX)$ ) and pitch ( $\theta_y(RX)$ ) angles of the RX. Compared to the 4DHT approach, the AMT approach tracked both TXs with higher density and precision.

Fig. 12 shows excerpts from experiments 4 to 6, including the  $y$ -coordinates of the TXs. Gray areas indicate when the blinking markers of the two TXs were close in the image, causing TX2 to be occluded by TX1. During these occlusions, signal crosstalk did not cause significant performance differences between the two algorithms.

Figure 13 presents excerpts of TX1’s fastest trajectories, highlighting the precision advantages of the AMT approach for agile multi-robot systems. For the slower linear trajectory, AMT achieved 81.71 % higher precision than 4DHT, which increased to 87.35 % during the faster trajectory. Similarly, in the circular trajectory, AMT demonstrated a 85.44 % precision advantage at  $2.57 \text{ m s}^{-1}$ , further improving to 89.28 % at  $4.06 \text{ m s}^{-1}$  compared to the 4DHT. In the “star” trajectory, AMT outperformed 4DHT by 84.90 % on the slower trajectory and by 83.37 % on the faster one.

Throughout all experiments, the AMT algorithm outperformed the 4DHT algorithm in tracking LED-IDs not facing the observer (0, 3, 4, and 7), achieving higher precision in distinguishing signals close to each other in the image. Tab. 2 shows that, on average, the AMT approach reduces computation time by 96.97% and memory usage by 86.31% compared to the state-of-the-art method. This substantial reduction in resource consumption frees up capacity for other onboard operations, making the AMT approach especially suitable for small onboard computers with limited resources. Overall, these results demonstrate

	AMT	4DHT
Avg. Computational Time ( $\bar{T}$ ) in [ms/f]	0.208	6.872
$\sigma(\bar{T})$	0.287	3.930
Avg. RSS ( $\overline{RSS}$ ) in [mB]	142.28	1039.61
$\sigma(\overline{RSS})$	12.11	197.10

Table 2: Average Computation Time per camera frame and RSS, with standard deviations, averaged over all experiments.

that the AMT approach excels in tracking fast, non-linear maneuvers, delivering enhanced precision through higher detection frequency and efficient resource use, making it ideal for agile multi-robot teams.

## 5. Conclusion

A novel approach, AMT, for extracting and tracking moving blinking light sources attached to multi-robot team members was introduced. The method was designed to satisfy the requirements and constraints of agile, compact swarming, tight formation flight, and high-speed multi-UAV operations. We demonstrated its performance in real-world outdoor experiments focusing on agile flight and tested the tracking of multiple UAVs on various trajectories, including linear and circular motions, as well as scenarios with mutual occlusions of the Transmitters. The algorithm surpassed the state-of-the-art method in tracking density, accuracy, and efficiency, significantly reducing computational and memory demands. The higher tracking density supports significantly faster relative motions, up to  $5 \text{ ms}^{-1}$ , making AMT ideally suited for agile multi-robot systems. Thus, we propose this approach as an enabling technology for mutual localization and omnidirectional low-bandwidth visual communication within agile Multi-UAV teams.

## References

- [1] S.-J. Chung, A. A. Paranjape, P. Dames, S. Shen, V. Kumar, A Survey on Aerial Swarm Robotics, *IEEE Transactions on Robotics* 34 (4) (2018) 837–855. doi:10.1109/TR0.2018.2857475.
- [2] S. Chen, D. Yin, Y. Niu, A Survey of Robot Swarms’ Relative Localization Method, *Sensors* 22 (12) (2022). doi:10.3390/s22124424.
- [3] H. Xu, L. Wang, Y. Zhang, K. Qiu, S. Shen, Decentralized Visual-Inertial-UWB Fusion for Relative State Estimation of Aerial Swarm, in: 2020 IEEE International Conference on Robotics and Automation (ICRA), IEEE, 2020. doi:10.1109/icra40945.2020.9196944.

- [4] Y. Gao, J. Yuan, J. Jiang, Q. Sun, X. Zhang, VIDO: A Robust and Consistent Monocular Visual-Inertial-Depth Odometry, *IEEE Transactions on Intelligent Transportation Systems* 24 (3) (2023) 2976–2992. doi:10.1109/TITS.2022.3226719.
- [5] C. Wu, S. Tu, S. Tu, L. Wang, W. Chen, Realization of Remote Monitoring and Navigation System for Multiple UAV Swarm Missions: Using 4G/WiFi-Mesh Communications and RTK GPS Positioning Technology, in: *2022 International Automatic Control Conference (CACs)*, 2022, pp. 1–6. doi:10.1109/CACS55319.2022.9969782.
- [6] W. Jiang, Z. Cao, B. Cai, B. Li, J. Wang, Indoor and Outdoor Seamless Positioning Method Using UWB Enhanced Multi-Sensor Tightly-Coupled Integration, *IEEE Transactions on Vehicular Technology* 70 (10) (2021) 10633–10645. doi:10.1109/TVT.2021.3110325.
- [7] J. P. Queralta, C. Martinez Almansa, F. Schiano, D. Floreano, T. Westerland, UWB-based System for UAV Localization in GNSS-Denied Environments: Characterization and Dataset, in: *2020 IEEE/RSJ International Conference on Intelligent Robots and Systems (IROS)*, IEEE, 2020, p. 4521–4528. doi:10.1109/iros45743.2020.9341042.
- [8] X. Zhou, X. Wen, Z. Wang, Y. Gao, H. Li, Q. Wang, T. Yang, H. Lu, Y. Cao, C. Xu, F. Gao, Swarm of micro flying robots in the wild, *Science Robotics* 7 (05 2022). doi:10.1126/scirobotics.abm5954.
- [9] F. Schilling, F. Schiano, D. Floreano, Vision-Based Drone Flocking in Outdoor Environments, *IEEE Robotics and Automation Letters* 6 (2) (2021) 2954–2961. doi:10.1109/LRA.2021.3062298.
- [10] X. Oh, R. Lim, S. Foong, U.-X. Tan, Marker-Based Localization System Using an Active PTZ Camera and CNN-Based Ellipse Detection, *IEEE/ASME Transactions on Mechatronics* 28 (4) (2023) 1984–1992. doi:10.1109/TMECH.2023.3274363.
- [11] F. J. Romero-Ramirez, R. Muñoz-Salinas, R. Medina-Carnicer, Speeded up detection of squared fiducial markers, *Image and Vision Computing* 76 (2018) 38–47. doi:https://doi.org/10.1016/j.imavis.2018.05.004.
- [12] T. Krajník, M. Nitsche, J. Faigl, T. Duckett, M. Mejail, L. Přeučil, External localization system for mobile robotics, in: *2013 16th International Conference on Advanced Robotics (ICAR)*, 2013, pp. 1–6. doi:10.1109/ICAR.2013.6766520.
- [13] H. Stuckey, L. Escamilla, L. R. Garcia Carrillo, W. Tang, Real-Time Optical Localization and Tracking of UAV Using Ellipse Detection, *IEEE Embedded Systems Letters* 16 (1) (2024) 1–4. doi:10.1109/LES.2023.3234871.

- [14] I. White, E. Curry, D. K. Borah, S. J. Stochaj, W. Tang, An Optical Spatial Localization Algorithm Using Single Temporal Difference Image Sensor, *IEEE Sensors Letters* 3 (3) (2019) 1–4. doi:10.1109/LSENS.2019.2900074.
- [15] L. Teixeira, F. Maffra, M. Moos, M. Chli, VI-RPE: Visual-Inertial Relative Pose Estimation for Aerial Vehicles, *IEEE Robotics and Automation Letters* 3 (4) (2018) 2770–2777. doi:10.1109/LRA.2018.2837687.
- [16] V. Walter, N. Staub, A. Franchi, M. Saska, UVDAR System for Visual Relative Localization With Application to Leader–Follower Formations of Multirotor UAVs, *IEEE Robotics and Automation Letters* 4 (3) (2019) 2637–2644. doi:10.1109/LRA.2019.2901683.
- [17] M. Faessler, E. Mueggler, K. Schwabe, D. Scaramuzza, A monocular pose estimation system based on infrared LEDs, in: 2014 IEEE International Conference on Robotics and Automation (ICRA), 2014, pp. 907–913. doi:10.1109/ICRA.2014.6906962.
- [18] J. Lim, T. Lee, S. Pyo, J. Lee, J. Kim, J. Lee, Hemispherical InfraRed (IR) Marker for Reliable Detection for Autonomous Landing on a Moving Ground Vehicle From Various Altitude Angles, *IEEE/ASME Transactions on Mechatronics* 27 (1) (2022) 485–492. doi:10.1109/TMECH.2021.3066643.
- [19] R. Jin, J. Wang, A vision tracking system via color detection, in: 2016 12th IEEE International Conference on Control and Automation (ICCA), 2016, pp. 865–870. doi:10.1109/ICCA.2016.7505387.
- [20] T.-H. Do, M. Yoo, Visible Light Communication-Based Vehicle-to-Vehicle Tracking Using CMOS Camera, *IEEE Access* 7 (2019) 7218–7227. doi:10.1109/ACCESS.2018.2890435.
- [21] M. Huang, W. Guan, Z. Fan, Z. Chen, J. Li, B. Chen, Improved Target Signal Source Tracking and Extraction Method Based on Outdoor Visible Light Communication Using a Cam-Shift Algorithm and Kalman Filter, *Sensors* 18 (12) (2018). doi:10.3390/s18124173.
- [22] I. White, D. K. Borah, W. Tang, Robust Optical Spatial Localization Using a Single Image Sensor, *IEEE Sensors Letters* 3 (6) (2019) 1–4. doi:10.1109/LSENS.2019.2919892.
- [23] D. Dias, R. M. M. Ventura, P. U. Lima, A. Martinoli, On-board vision-based 3D relative localization system for multiple quadrotors, 2016, pp. 1181–1187.
- [24] H. Stuckey, A. Al-Radaideh, L. Escamilla, L. Sun, L. G. Carrillo, W. Tang, An Optical Spatial Localization System for Tracking Unmanned Aerial Vehicles Using a Single Dynamic Vision Sensor, in: 2021 IEEE/RSJ International Conference on Intelligent Robots and Systems (IROS), 2021, pp. 3093–3100. doi:10.1109/IROS51168.2021.9636665.



- [25] H. Stuckey, A. Al-Radaideh, L. Sun, W. Tang, A Spatial Localization and Attitude Estimation System for Unmanned Aerial Vehicles Using a Single Dynamic Vision Sensor, *IEEE Sensors Journal* 22 (15) (2022) 15497–15507. doi:10.1109/JSEN.2022.3187423.
- [26] G. Chen, T. Wu, F. Yang, T. Wang, J. Song, Z. Han, Ultraviolet-Based UAV Swarm Communications: Potentials and Challenges, *IEEE Wireless Communications PP* (2022) 1–8. doi:10.1109/MWC.007.2100405.
- [27] G. Ryou, E. Tal, S. Karaman, Cooperative Multi-Agent Trajectory Generation with Modular Bayesian Optimization, in: *Proceedings of Robotics: Science and Systems, 2022*. doi:10.15607/RSS.2022.XVIII.060.
- [28] A. Breitenmoser, L. Kneip, R. Siegwart, A monocular vision-based system for 6D relative robot localization, in: *2011 IEEE/RSJ International Conference on Intelligent Robots and Systems, 2011*, pp. 79–85. doi:10.1109/IRoS.2011.6094851.
- [29] A. Censi, J. Strubel, C. Brandli, T. Delbruck, D. Scaramuzza, Low-latency localization by active LED markers tracking using a dynamic vision sensor, in: *2013 IEEE/RSJ International Conference on Intelligent Robots and Systems, 2013*, pp. 891–898. doi:10.1109/IRoS.2013.6696456.
- [30] G. Ebmer, A. Loch, M. N. Vu, R. Mecca, G. Haessig, C. Hartl-Nesic, M. Vincze, A. Kugi, Real-time 6-DoF Pose Estimation by an Event-based Camera using Active LED Markers, in: *2024 IEEE/CVF Winter Conference on Applications of Computer Vision (WACV), 2024*, pp. 8122–8131. doi:10.1109/WACV57701.2024.00795.
- [31] V. Walter, M. Saska, A. Franchi, Fast Mutual Relative Localization of UAVs using Ultraviolet LED Markers, in: *2018 International Conference on Unmanned Aircraft Systems (ICUAS), 2018*, pp. 1217–1226. doi:10.1109/ICUAS.2018.8453331.
- [32] L. Gorse, C. Löffler, C. Mutschler, M. Philippsen, Optical Camera Communication for Active Marker Identification in Camera-based Positioning Systems, in: *2018 15th Workshop on Positioning, Navigation and Communications (WPNC), 2018*, pp. 1–6. doi:10.1109/WPNC.2018.8555846.
- [33] V. Walter, N. Staub, M. Saska, A. Franchi, Mutual Localization of UAVs based on Blinking Ultraviolet Markers and 3D Time-Position Hough Transform, in: *2018 IEEE 14th International Conference on Automation Science and Engineering (CASE), 2018*, pp. 298–303. doi:10.1109/COASE.2018.8560384.
- [34] P. Petráček, V. Walter, T. Báča, M. Saska, Bio-inspired compact swarms of unmanned aerial vehicles without communication and external localization, *Bioinspiration & Biomimetics* 16 (2) (2020) 026009. doi:10.1088/1748-3190/abc6b3.

- [35] J. Horyna, V. Walter, M. Saska, UVDAR-COM: UV-Based Relative Localization of UAVs with Integrated Optical Communication, in: 2022 International Conference on Unmanned Aircraft Systems (ICUAS), 2022, pp. 1302–1308. doi:10.1109/ICUAS54217.2022.9836151.
- [36] D. B. Licea, V. Walter, M. Ghogho, M. Saska, Optical Communication-Based Identification for Multi-UAV Systems: Theory and Practice. arXiv:2302.04770, doi:10.48550/arXiv.2302.04770.
- [37] R. A. Serway, C. J. Moses, C. A. Moyer, Nuclear Structure, in: Modern Physics, 3rd Edition, Thomson Brooks/Cole, 2005, pp. 463–502.
- [38] G. H. Golub, C. F. V. Loan, Matrix Computations, JHU Press, 1996. arXiv:m10a7wPX60YC.
- [39] G. Seber, A. Lee, Computational Algorithms for Fitting and Regression, in: Linear Regression Analysis, Wiley, 2003, pp. 329–389. doi:10.1002/9780471722199.ch11.
- [40] S. M. Ross, Chapter 9 - Regression, in: S. M. Ross (Ed.), Introduction to Probability and Statistics for Engineers and Scientists (Fifth Edition), Academic Press, 2014, pp. 357–444. doi:10.1016/B978-0-12-394811-3.50009-5.
- [41] D. Hert, et al., Mrs drone: A modular platform for real-world deployment of aerial multi-robot systems, Journal of Intelligent & Robotic Systems 108 (4) (Jul. 2023). doi:10.1007/s10846-023-01879-2.